LLNL-JRNL-848642

LAWRENCE
LIVERMORE
NATIONAL
LABORATORY

Explosive fragmentation of additively manufactured stainless steel

M. Callahan, D. Sun, M. Linne, G. Campbell, H. S. Park, B. Friedman, J. Rodriguez, S. Burke, A. Lodes, K. Hansen, K. Mickelson, R. Wraith, A. Wu

May 3, 2023

Journal of Applied Physics

Disclaimer

This document was prepared as an account of work sponsored by an agency of the United States government. Neither the United States government nor Lawrence Livermore National Security, LLC, nor any of their employees makes any warranty, expressed or implied, or assumes any legal liability or responsibility for the accuracy, completeness, or usefulness of any information, apparatus, product, or process disclosed, or represents that its use would not infringe privately owned rights. Reference herein to any specific commercial product, process, or service by trade name, trademark, manufacturer, or otherwise does not necessarily constitute or imply its endorsement, recommendation, or favoring by the United States government or Lawrence Livermore National Security, LLC. The views and opinions of authors expressed herein do not necessarily state or reflect those of the United States government or Lawrence Livermore National Security, LLC, and shall not be used for advertising or product endorsement purposes.

Explosive fragmentation of additively manufactured stainless steel

M. Callahan, D. Sun, M.A. Linne, A.S. Wu*, G.H. Campbell, B. Friedman, J. Rodriguez, S. Burke, A. Lodes, K. Hansen, K. Mickelson, R. Wraith, J. Wang Nicolino, H.-S. Park
Lawrence Livermore National Laboratory, 7000 East Avenue, Livermore CA 94550
**Corresponding author:* wu36@llnl.gov

Abstract

Properties of fragmentation from an explosively driven 316L stainless steel spherical shell section fabricated by a laser powder bed additive manufacturing process with minimal surface finishing are investigated. This shell is driven by an insensitive high explosive, resulting in high strain rate deformation (>$8x10^3$ s^{-1}) and failure of the stainless steel. Photonic doppler velocimetry measures the expansion rate; dynamic radiography and high-speed imaging capture the fracture behavior of the stainless steel. The fracture response of the additively manufactured stainless steel shell is compared to published experimental results on additively manufactured 316L stainless steel and conventionally manufactured wrought 316L and 304 stainless steel shell fragmentation. Despite a preferred crack orientation, suggesting the influence of surface grooves on fracture time, fragment size is identical to that measured in a similar experiment on wrought 304 stainless steel. Further analysis indicates that the 316L additively manufactured stainless steel shell exhibits comparable spall strength and fragmentation toughness to conventionally manufactured stainless steel, yet lower failure strain due to surface stress concentrations.

Keywords: additive manufacturing, stainless steel, fragmentation, explosive loading, dynamic testing

1. Introduction

Explosively driven fragmentation introduces a distinct set of high strain rate loading conditions with applications in commercial and military sectors. The study of material failure in a regime dominated by kinetic energy contributions provides unique opportunities for defect analysis and material model development. The experiment described herein is aimed at assessing the role of regular surface defects on the dynamic fragmentation behavior of a metal spherical shell section produced by additive manufacturing (AM).

Fragmentation behavior of metals has been broadly studied. Griffith's energy balance analysis of surface crack growth in an elastic body, i.e., balancing stored strain energy and applied work with the energy required to create new surfaces [1], has formed the foundation for modern fracture mechanics, as reviewed by Lawn [2]. In ductile metals, rupture occurs by the growth and coalescence of microvoids [3, 4] which nucleate at internal defects [5-7], rather than at the surface as in Griffith's elastic body. In 1947, Mott published a statistics-based approach to describe the dynamic fragmentation of ductile metal rings; cracks open at random locations and reflections at the free surface produce release waves that relieve local tension and prevent further fragmentation within the release wave field. In this analysis, Mott related fragment size to the true stress, plastic strain, strain hardening rate, and density [8].

Mott's approach was refined and reviewed by Grady [9], who developed energy-based analyses of ductile metal fragmentation during explosive loading [10, 11]. Grady's analysis covered a broad range of topics including shear band formation, thermally enhanced ductility, balancing inertial forces and surface tension to determine fragment size, and the experimental validation of such approaches [12-14]. The dynamic properties of stainless steel were discussed in the context of ball on plate impact experiments [12], analysis of which resulted in fragmentation toughness values ranging from 80-100 MPa-m$^{1/2}$ in 304 stainless steel and critical strain of 0.38.

Substantial investigations into metal cylinders expanded by internal pressure [15-20] have been made based on an analysis of fragment velocities by Gurney [21], more legible version by Jones *et al.* [22], and Taylor [23]. Conical impact loaded by a gas gun as an alternative to cylindrical fragmentation [24] generates fragmentation data of comparable quality. These studies largely focused on providing information on the fragment size distribution and examining the failure mechanisms present in these tests. In 2003, Grady advanced his formulations to describe the dynamic fragmentation of an expanding metal shell [25].

Extension of these analyses to develop simulation tools capable of describing fragmentation behavior has been a focus of literature during the recent two decades. In 2000, Wilson *et al.* implemented the Grady-Kipp fragmentation model into the CTH Shock Physics Code [26, 27], simulating published experiments on AerMet 100 steel (13.4wt% Co, 11.1wt% Ni, 3.1wt%Cr, 1.2wt%Mo, 0.23wt%C, and Fe balance, for more details see [28]) and 90% tungsten alloy in the exploding cylinder configuration [29]. In 2004, Syn *et al.* measured the impact response of AerMet 100 steel for the purpose of validating a Steinburg-Guinan based hydrodynamics code (CALE) [30]. Tsuji *et al.* [31] employed meshfree smoothed particle hydrodynamics in Arbitrary Lagrangian–Eulerian three-dimensional analysis (ALE3D), applying this simulation method to the experimental data described by Syn *et al.* [30]. In 2007, Campbell *et al.* used numerical and analytical approaches to describe dynamic fragmentation of a spherical shell comprised of 304 stainless steel [32]. In Campbell's experiment, fragments were recovered and analyzed to determine the fragmentation energy of 304 stainless steel.

Goto *et al.* [16] further refined the hydrodynamics code from Syn *et al.* [30], using a Johnson-Cook fracture model validated on experiments of AerMet® 100 steel alloy and AISI 1018 steel explosively driven rings and cylinders. Similar to Campbell *et al.*, their analysis included capture and measurement of fragment sizes. Hopson et al. employed a Weibull distribution function to randomize failure strain within the Johnson-Cook fragmentation model and reported analysis based on prior data collected for explosively driven AerMet® 100 steel cylinders [33]. Similar analysis of explosively driven cylinders has been performed for other metals, including tungsten alloy Aero-224 and Eglin Steel (ES-1) [34], A235 steel [35], and 45# steel [36].

Here, analysis was performed to understand the dynamic fragmentation behavior of additively manufactured 316L stainless steel with minimal surface finishing. Additive manufacturing offers a platform supportive of creative design which is routinely used to produce functional systems for commercial applications [37-44]. The expansion of industrial applications for AM has prompted studies into AM materials performance under increasingly broad and more extreme performance environments and loading conditions. AM methods, specifically the laser powder bed fusion process, can introduce unique microstructures with a broader array of defects (inclusions and porosity) than observed in conventionally manufactured metal. Fragmentation is known to depend on the applied strain rate [7, 45] as well as the stress triaxiality [46-48] and the defect population in the sample—i.e. pre-existing pores or brittle inclusions, which fracture or debond from the crystal lattice under applied load, create void nucleation sites. The rate of pore growth depends not solely on the strain rate and stress state, but also on the location of the pore in the sample. For example, it has been shown that in fatigue, surface defects are much more influential in seeding fracture than those in the core of the sample [49]. In uniaxial tension the opposite tends to be true [50]. When the strain rate increases such that inertial effects become relevant, however, these trends do not necessarily hold up.

Plastic strain can be accommodated by various mechanisms depending on the applied strain rate. In general, quasi-static loading—when the strain rate is slow enough that inertial effects become negligible—tends to plastically strain by thermally-activated mechanisms such as dislocation slip or grain boundary creep. For dynamic loading—where inertial effects become important—fast mechanisms such as shear banding, twinning, or strain-induced phase transformations dominate. Such highly localized deformation mechanisms can lead to more brittle behavior and, depending on the defect population in the sample, can result in more stochastic failure behavior compared to that observed under quasi-static conditions [51]. Factors affecting the rate dependent resistance of metals to plastic flow and factors contributing to dynamic crack growth are discussed in detail by Gilman [52] and the transition from lattice or defect control to phonon drag control [53] is relevant at the strain rates accessed during this experiment. Remington *et al.* discuss experiments into plastic flow at pressures from 100-500 GPa and strain rates from 10^6 to 10^8 s^{-1} [54].

Relatively few fragmentation studies have looked at the influence of defects on the fragmentation process. Liang et. al. [55] performed cylindrical fragmentation experiments with U-notches between 1 mm and 6 mm deep on both the internal and external surfaces of the samples and reported a clear effect on fragment size. Wood et. al. performed a study on AM Inconel 718 containing internal porosity of various sizes [56]. They demonstrated that coalescence tends to be dominated by the largest pores and that ductile dimples tend to be quite shallow, suggesting that the rapid loading in explosively driven experiments does not provide time for any appreciable void growth. This is confirmed by simulations performed by Fick *et al.*, who demonstrated that void growth only occurred for 50 ns in a 200 ns experiment before quickly ceding to rapid void coalescence [57]. They also demonstrated a negligible effect of adiabatic heating, again due to the extremely brief duration of plastic strain and fragmentation.

Koube *et al.* recently investigated the effect of pore size and spacing on the spall behavior of AM 316L stainless steel [58-60]. Their plate on plate impact study provides experimental data from which an independently measured fracture toughness of AM 316L stainless steel, acquired under dynamic loading conditions, may be extracted following the method described by Buchar *et al.* [61].

This study examines the influence of external defects on the fragmentation behavior of an AM 316L stainless steel shell through explosively driven biaxial tension experiments that reach a tensile strain rate or stretching rate of up to 8000-9000 s^{-1}. A sample with process-induced surface defects was manufactured to observe the influence of small surface stress concentrations. Furthermore, an overall comparison of the performance of AM 316L stainless steel shell with dynamic experiments on AM 316L and wrought 304 are made. Analysis of the current experiment provides localized information, such as applied strain rate and failure strain.

2. Experimental methodology

2.1 Materials selection

In this study, the performance of AM 316L is compared with that of similarly manufactured material, as well as wrought-processed stainless steel. This section is dedicated to describing the chemistry and mechanical properties of these alloys to facilitate later comparisons.

Austenitic stainless steel types 304 and 316L are known for their excellent fracture resistance, as measured up to 550C, and a comprehensive study of the two alloys and effects of heat to heat variability was conducted by Mills [62]. These alloys deform similarly and are primarily distinguished by the enhanced corrosion resistance imparted by the additional alloying content of 316L (Ni and Mo).

The role of build parameter optimization on porosity in AM 316L has been studied by others, see Garlea *et al*. [63]. The role of heat treatment on toughening in selective laser melted (SLM) 316L has been reported by Davies *et al.* [64] and Wang *et al*. [65]. Ductile dimpled fracture was consistently observed, indicative of microvoid coalescence (MVC), which is the typical fracture mechanism in 316L and 304 stainless steels. Heterogeneity introduced by AM can influence fracture toughness, leading to significant sample to sample variation and build direction anisotropy [66]. Literature values for yield stress (σ_y) ultimate tensile strength (σ_{uts}), failure strain (ε), and fracture toughness ($J_{0.2}$) for AM 316L, wrought 316L, and wrought 304 are provided in Table 1. This data indicates that post build heat treatment can improve ductility and fracture toughness.

Table 1. Room temperature composition and mechanical properties of 304 and 316L stainless steels by manufacturing process

Alloy	Manufacture	Heat treatment	Composition												Rel	σ_y	σ_{uts}	ε	$J_{0.2}$	Ref
			Cr	Ni	Mo	Mn	Si	N	C	P	S	Cu	O	Fe	(%)	(MPa)	(MPa)	(%)	(KJ/m^2)	
304	wrought		17.5-19.5	8-10.5	-	≤2	≤1	≤0.11	≤0.07	≤0.05	≤0.03	-	-	bal		≥205	≥515	≥40	300	[62]
316L	wrought		16-18	10-14	2-3	≤2	≤0.75	≤0.1	≤0.03	≤0.045	≤0.03	-	-	bal		≥205	≥515	≥60	260-280	[62]
316L	SLM 250^{HL}	as-built/ SLM surface	17.03	10.52	2.27	-	-	-	0.018	-	-	-	-	bal		462	565	53.7		[67]
316L	Concept M2	as built	-	-	-	-	-	-	-	-	-	-	-	-	98.80	590±17	705 ± 15	44 ± 7		[68]
316L	Renishaw AM250	as built	17.9	12.7	2.36	1.45	0.67	0.06	0.019	0.019	0.006	0.2	0.022	bal	98.04	385	524	22		[69]
316L	FS271 M	as built	16.97	12.01	2.53	1.48	-	-	-	-	-	-	-	bal		590±10	655 ± 10	45 ± 2	275.7	[70]
316L	SLM 125^{HL}	as built	16.8	12	2.5	1.25	0.56	0.048	0.014	-	-	-	0.036	bal	>99.5	400.3±3.1	572.8 ± 0.6	45.5 ± 0.3		[71]
316L	FS271 M	400C 3h	16.97	12.01	2.53	1.48	-	-	-	-	-	-	-	bal		580±10	700 ± 10	43 ± 2	270.1	[70]
316L	SLM 250^{HL}	650C 2h	17.03	10.52	2.27	-	-	-	0.018	-	-	-	-	bal		443	595	48.6		[67]
316L	SLM 280^{HL}	900C 1h	17.7	11.9	2.4	0.8	0.4	0.09	0.019	-	-	-	0.03	bal	99.70	400-410	590-690		300-550	[66]
316L	SLM 280^{HL}	900C 1h	16.6	12	2.6	1.2	0.6	0.01	0.004	-	-	-	0.08	bal	99.70	330-340	580-610		350-575	[66]
316L	Concept M2	1095C 1h	-	-	-	-	-	-	-	-	-	-	-	-	98.80	375±11	635 ± 17	51 ± 3		[68]
316L	SLM 125^{HL}	1100C 0.5h	16.8	12	2.5	1.25	0.56	0.048	0.014	-	-	-	0.036	bal	>99.5	307.8±3.0	546.1 ± 2.3	54.5 ± 1.6		[71]
AM homogenized summary																307.8-410	540-690	48.6-57.5	300-575	
316L	Concept M2	1000C 1h, 850C 0.5h	17.7	12.7	2.36	0.65	0.62	0.1	0.022	0.007	0.005	0.02	0.03	bal						This study

*Note that specimens are all tested in the finish machined condition except where “SLM surface” is noted.

2.2 Hydrodynamic sample fabrication

A 316L stainless steel spherical shell section was manufactured using a SLM® 280 (SLM Solutions) laser powder bed fusion AM machine using standard build parameters for 316L stainless steel, i.e., laser power of 175 W and laser speed of 850 mm/s, similar to those found in literature [72, 73]. The shell was overbuilt by 1 mm on all sides, except the convex surface, to facilitate machining down to the desired surface finish of 1.6 µm Ra. Inner and side surfaces were finish precision-machined, rather than kept as-built, to ensure proper fit and alignment with the test fixturing and to achieve a constant adhesive layer thickness between the concave surface and the high explosive.

Prior to machining, the build was homogenized in an argon atmosphere at 1000°C for 1 hour, cooled to 850°C, and then quenched to room temperature using forced air to obtain a retained austenite microstructure. The concave side of the shell (upper surface of the build) was machined while still on the build plate for easier mounting in the lathe. After this step, the cap was removed from the build plate using wire electrical discharge machining. After final machining, the shell measured 198.05 mm inner radius of curvature, and 2.95 mm in shell thickness, similar to that described in a study by Campbell *et al.* [32].

The convex surface of the shell was intentionally left unmachined to test the effect of a realistic, AM surface finish. To achieve this, the support structure was manually torn from the convex surface and deburred by hand using 200 grit sandpaper. After that, no further machining was performed on this surface. This approach resulted in a rough surface with a checkerboard pattern of regular grooves formed upon support structure removal, spaced 1 mm apart (Fig. 1). The grooves were inspected using a Zygo NX2 3D coherence scanning interferometric profiler which reported an average groove width of 69±7 µm and depth of 147±23 µm (Fig. 2).

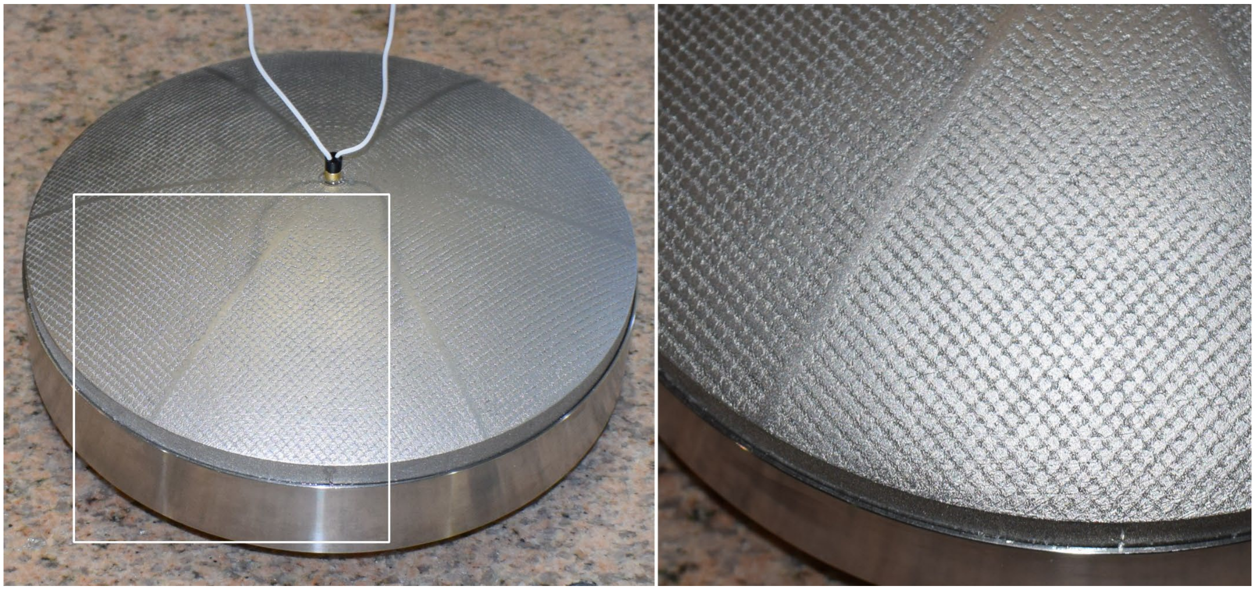

Fig. 1. Photographs of the spherical shell illustrating the external grooves left by support structure removal. Unfinished surface show grooves of ~69 µm width with 147 µm depth.

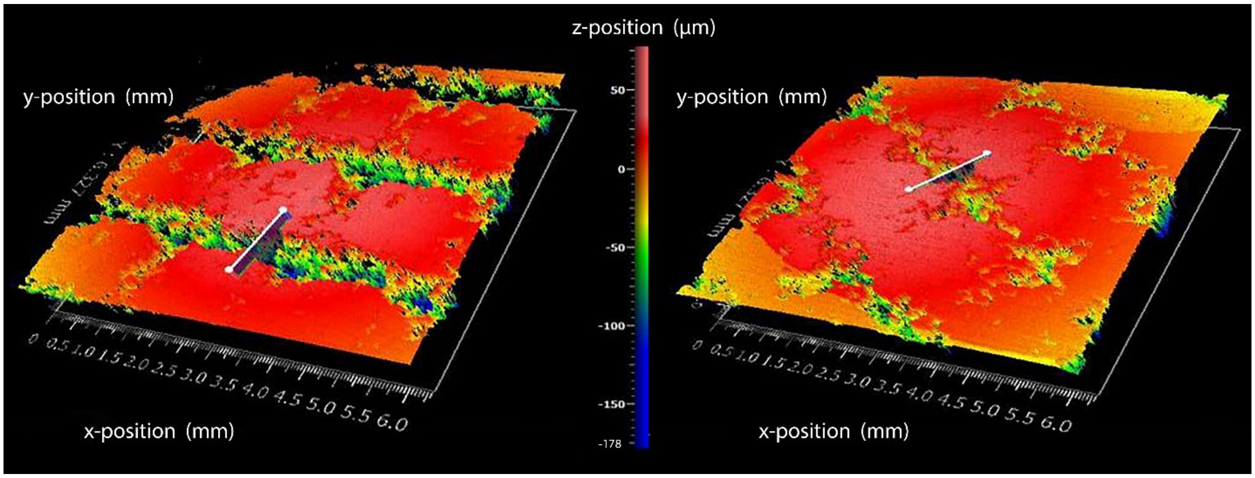

Fig. 2. 3D color maps illustrating surface height variation in two randomly inspected regions. Measurement locations are indicated by the white lines.

2.3 Experimental assembly

A 30.0 mm thick, 1.45 kg (1.3 kg TNT equivalent) spherical shell section of LX-17 high explosive was glued to the concave surface of the 316L stainless steel spherical shell and fixed in place using a stainless steel cylinder, as illustrated in Fig. 3. A dome-shaped booster charge of LX-10 high explosive was placed in a recess at the center of the LX-17 charge and an RP-2 exploding-bridgewire (EBW) detonator, manufactured by RISI, was mounted in a hole in the stainless steel shell and glued in place. The main charge, LX-17, is comprised of 92.5 wt.% 1,3,5-triamino-2,4,6-trinitrobenzene (TATB), bonded by 7.5 wt.% polychlorotrifluoroethylene (PCTFE, known as Kel-F®) and the booster charge, LX-10, is comprised of 95 wt.% octahydro-1,3,5,7-tetranitro-1,3,5,7-tetrazocine bonded by 5 wt.% fluoropolymer (Viton^{TM} A-100); further details on these high explosives can be found in the literature [74, 75].

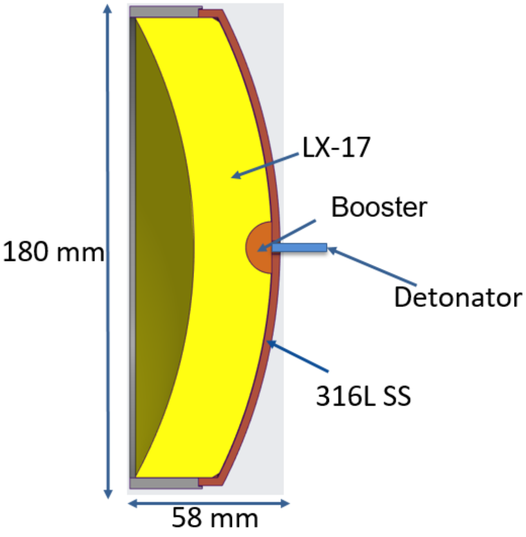

Fig. 3. The sample assembly was comprised of the 316L stainless steel spherical shell, LX-17 high explosive, LX-10 booster charge. The locations of the booster and detonator are indicated on the schematic.

2.4 Radiography

The layout of the experiment is provided in Fig. 4. A 2.3 MeV X-ray source was positioned 2.4 m upstream from the sample assembly, which was mounted into a foam board supported by an aluminum frame. An aluminum case containing a stack of 8 phosphor films was positioned 1.2 m downstream from the sample, and a 6.35 mm thick aluminum blast shield was placed between the sample and phosphor stack to mitigate sample fragment damage to the phosphor stack. Two 0.36 x 0.43 m (14 x 17 in) image plates were stacked side-by-side (0.43 x 0.71 m in total size) to capture the entire fragmentation event at the radiograph time. The radiograph acquisition time was 60.12 μs after detonator break out.

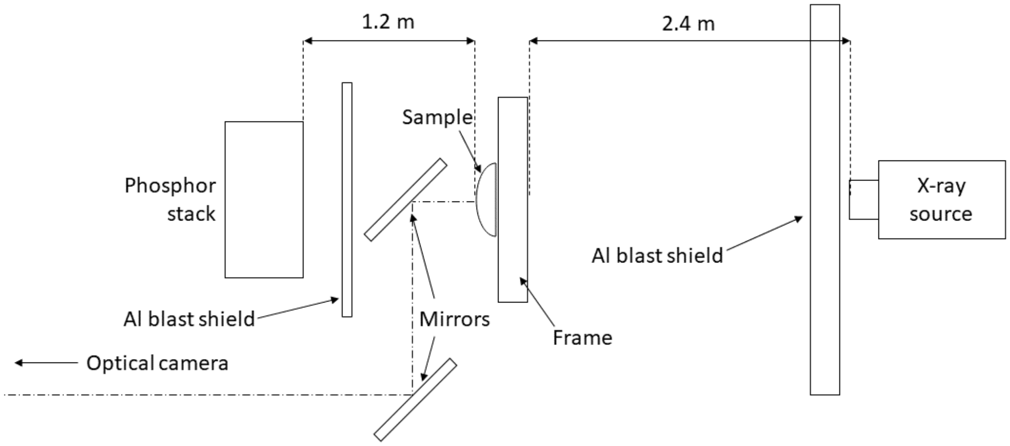

Fig. 4. Schematic of the experimental layout. The sample assembly was placed 2.4 m from the X-ray source, facing towards the phosphor stack which was 1.2 m downstream. An aluminum blast shield protects the phosphor stack from fragments, and a series of mirrors direct an image of the sample surface to an optical camera set up a safe distance from the blast zone.

2.5 Velocimetry

Surface velocity of the stainless steel shell was measured using four photonic Doppler velocimetry (PDV) probes. These were fixed in place using a plastic arm manufactured using a fused deposition modeling 3D printer. The arm was designed to align each PDV probe beam perpendicular to the surface of the shell, as illustrated in Fig. 5. Four probes (labeled 2-5 in Fig. 5) were used to increase the chances of obtaining high-quality data, as the measurements can be affected or even cut off entirely by spallation of the sample surface or by the cloud of detonation by-products. The timing of each PDV trigger was adjusted by 1.65 μs to account for the delay between the detonation signal and actual break out of the detonation wave in the explosive booster.

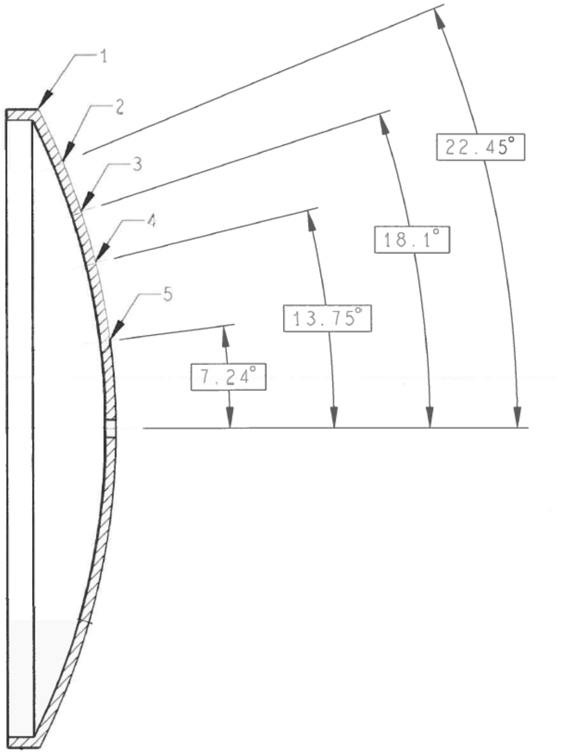

Fig. 5. Spherical shell diagram illustrating PDV probe locations, with outer edge marked 1 and probe locations marked 2-5 from outer edge to center.

2.6 High-Speed Optical Imaging

High-speed optical images were acquired using two series of mirrors placed between the sample and the phosphor stack such that the image of the convex surface of the sample was reflected to a Specialized Imaging SIMX/SIM16 framing camera. This camera used a rotating mirror to acquire up to 16 frames at a frame rate up to 10^6 frames per second. The resolution of the sensors was 1360 x 1024 pixels with a 390 mm x 300 mm field-of-view. Four MegaSun modular surface discharge flash lamps outputting 5 kW/cm^2 of irradiance provided sufficient illumination for the experimental rate of 5 x 10^5 frames per second.

3. Results

3.1 Radiography

A dynamic radiograph of the shell fragmentation is shown in Fig. 6 . The image is inverted such that lighter color corresponds to increasing x-ray opacity. The center of the image appears lighter due to convergence of the HE detonation products on axis of the experiment and reduced x-ray transmission. The horizontal bar spanning the bottom of the radiograph is a plate that acts as a blast shield for the calibration steps. In the bottom right quadrant of the image, the plastic arm holding the PDV probes is visible with bright spots at the locations of the probes themselves. The partial ring of fragments towards the outer edges of the image are from the stainless steel sleeve that the sample was placed into to maintain alignment during assembly. Each image plate is 1780x2156 px or 232 x 281 mm, as measured using static radiography.

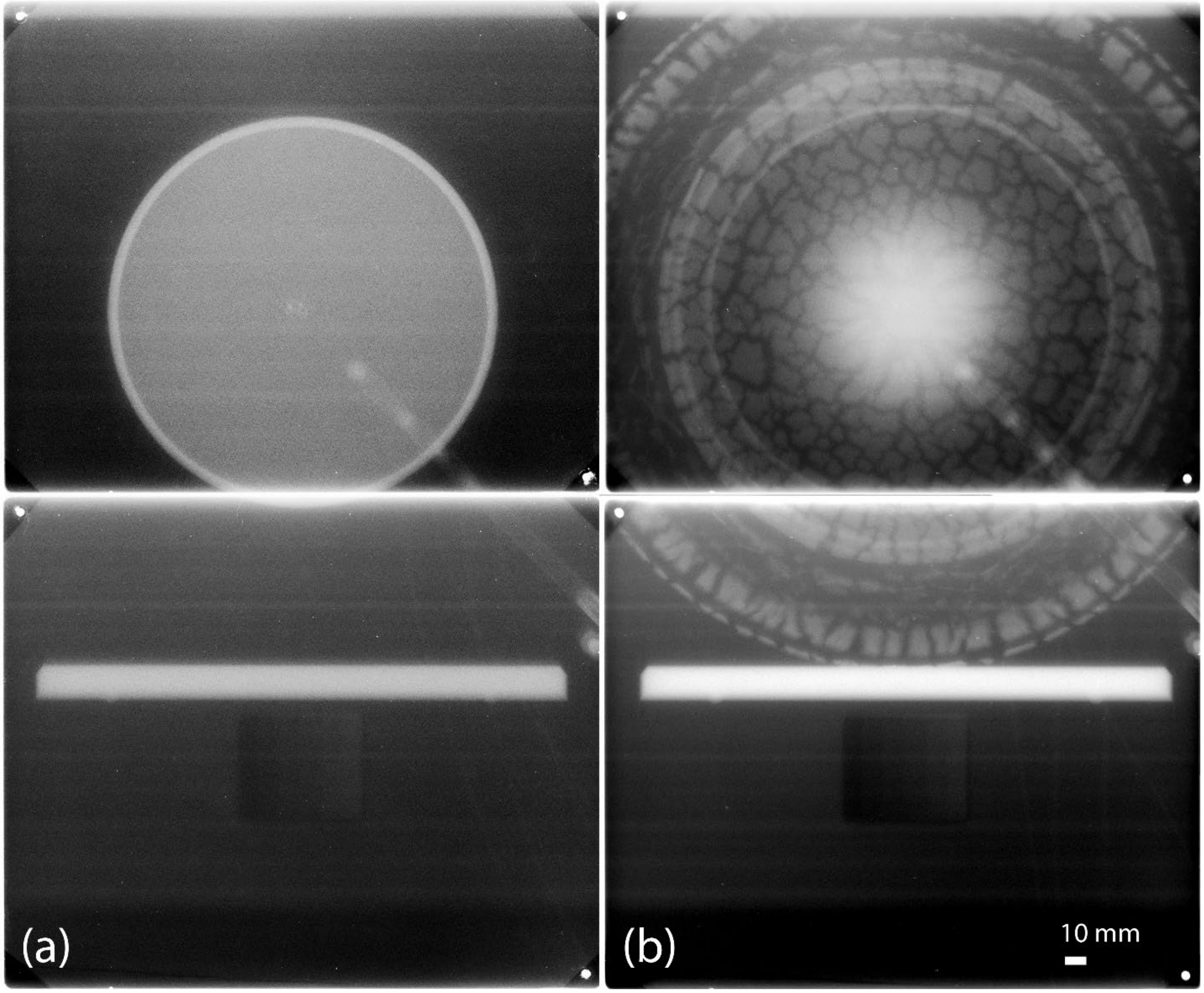

Fig. 6. (a) Static experimental radiograph acquired prior to detonation and (b) dynamic experimental radiograph acquired 60.12 μs after detonation.

3.2 Optical Imaging

Optical images acquired after detonation are shown in Fig. 7. From 7.6 to 14.6 μs after detonation trigger, the initial blast wave can be seen propagating outward from the center of the sample. A black plume of smoke can be seen erupting from the detonator location at the center of the shell. In the bottom right corner of each image, a black structure containing the four PDV probes is visible. Between 5.6 μs and 16.6 μs a light grey circle is seen propagating outward from the center of the sample; this is the shock wave propagation moving out from the detonation point and distorting the shape of the sample, causing it to reflect light differently in the deformed region. Shortly after, starting from 12.6 μs, a much darker shape begins to appear in the center of the sample and corresponds to a plume of smoke erupting from the hole into which the detonator was placed. Starting at 16.6 μs, a bright ring of explosive smoke is visible emanating from behind the sample and spreading in a ring around it.

Of note is the appearance of surface cracks starting at 32.6 μs, which are visible just behind the PDV array in the bottom right of the frame. The black lines denoting the cracks are plumes of high explosive detonation products being forced out through the cracks once it fully penetrates the thickness of the sample. As this is the first observed evidence of failure in this sample, the approximate fracture initiation time is t_f=28.6-32.6 µs. In the subsequent frames—particularly at 36.6 µs—cracks are seen to appear throughout the sample and tend to follow the directionality of the surface unfinished pattern quite closely. It is clearly notable that the cracks take on an orthogonal pattern that aligns with the grid structure left behind by the build's support structure. The final frame was taken at a time coincident with the firing of the radiograph, and in this frame the sample is completely hidden behind a cloud of high explosive detonation products.

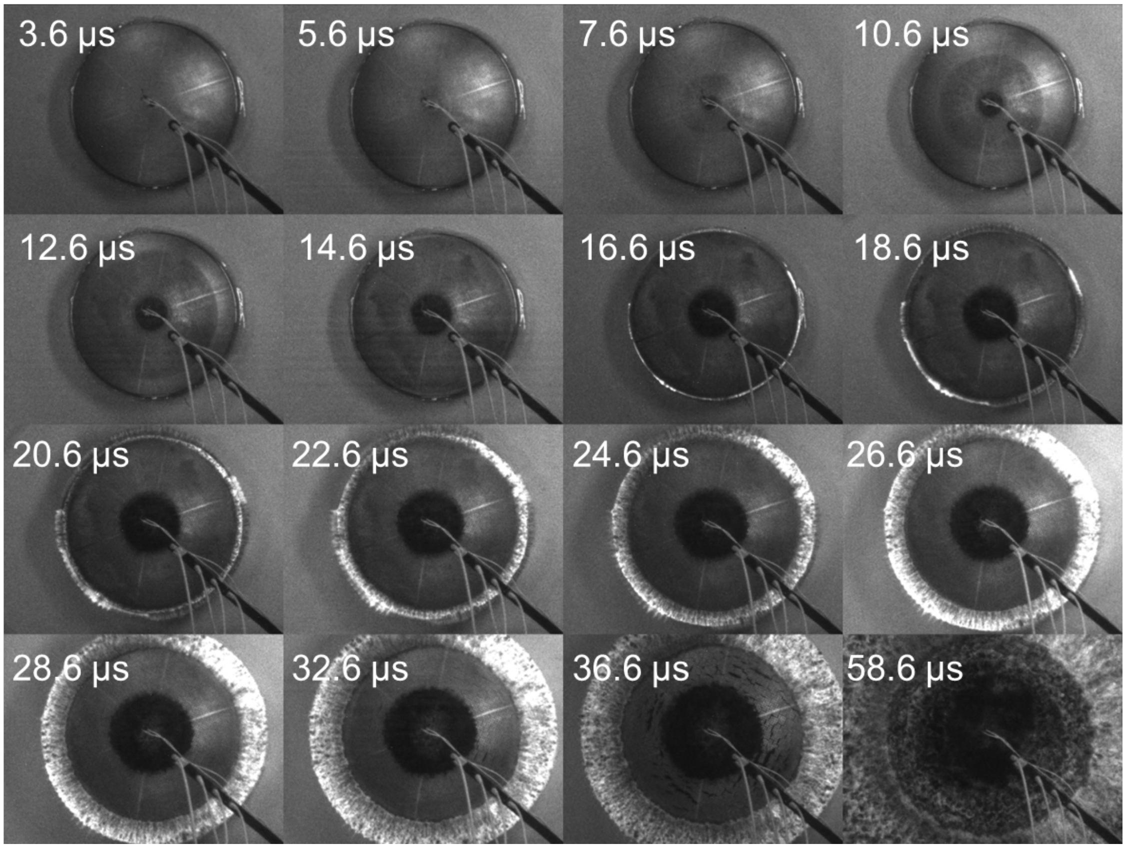

Fig. 7. High speed photographs of the spherical shell with time after the detonation trigger indicated on each tile of the mosaic.

3.3 Velocimetry

The expansion rate of the shell, plotted in Fig. 8, was measured in the four locations indicated in Fig. 5. After initial velocity jump off, a pullback or decrease in velocity associated with wave reflection and spall was observed at each probe location. A terminal velocity of 1700 m/s was estimated based on extrapolation of the data from the probe at location 4 (based on a logistic data fit with asymptote at 1707 m/s). The centermost and outermost probe traces were likely obscured by smoke as indicated in Fig. 7. It is not immediately evident why the probe signal at location 3 was terminated at 18 µs; it may be due to signal interruption from surface fracture, which is evident at this location at later times (Fig. 7, 32.6 µs frame).

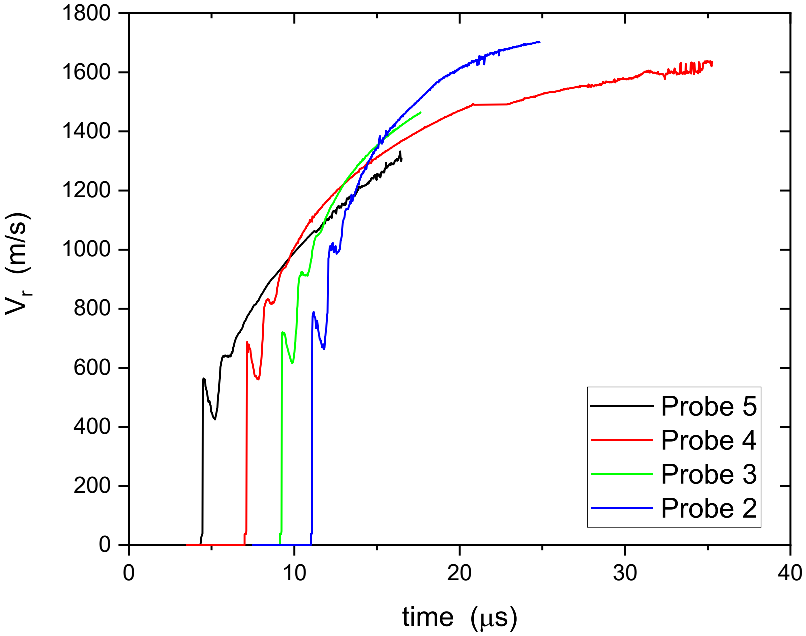

Fig. 8. Plot of velocimetry at four locations along the shell radius; the Probe at location 5 (see Fig. 5 for reference) is the innermost probe toward the center.

4. Analysis and Discussion

This experiment was performed to understand and predict the fragment size and dynamic mechanical properties of AM stainless steel under explosive loading conditions. Fragment size can be directly measured via radiography; a radiography time of 60 μs after detonator trigger was chosen in order to capture the majority of fragments on a single film based on simulated expansion velocity. Based on the measured radial velocity progression from the PDV data, it appears that terminal velocity is reached by this time. Due to the absence of further fragment loading and stress relief upon fragment formation, the radiographically measured fragment size should provide a reasonable representation of fragment size at later times to facilitate comparison with experimental results from literature.

4.1 Radiographic Analysis

Fragment sizes were measured in an annular region of the spherical shell (Fig. 9a) to ensure measurements represent material subjected to biaxial tension. Fig. 9b shows the radiograph with a mask applied to show this region of interest. Fragments identified by the watershed process are shown in Fig. 9c implemented using the MorpholibJ package [76] of open-source image analysis software ImageJ [77]. These segmentation results were used to determine the fragment size distribution, shown in Figure 10. Partial fragments, intersecting the edge of this region of interest, were excluded from the fragment size distribution.

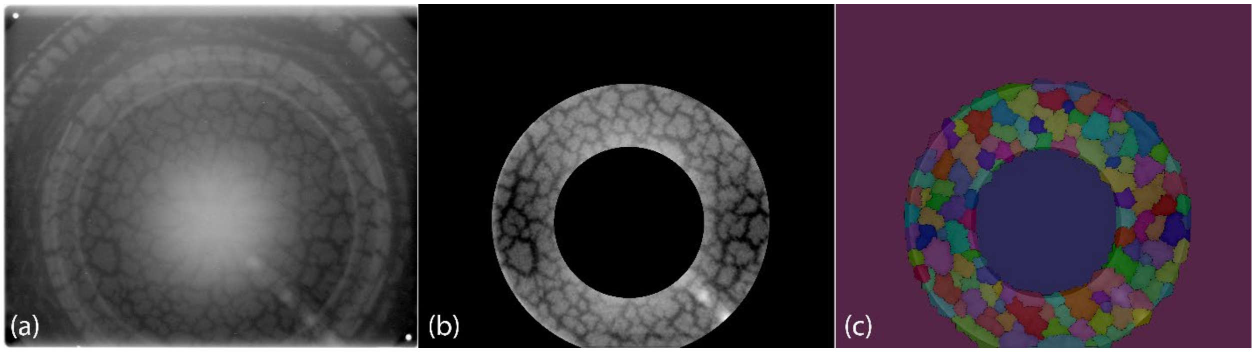

Fig. 9. (a) Dynamic radiograph with (b) mask applied to highlight region of interest and (c) color labeling of individual fragments.

The fragment distribution was compared to a published hydrodynamic test of a wrought 304 stainless steel spherical shell [32]. In this prior experiment, no dynamic radiograph was acquired, rather fragments were recovered after a shot and analyzed to directly measure the failure strain of 304 stainless steel and fragment sizes. The 304 stainless steel shell was detonated using a different high explosive than the one used here; however, the mass of the current explosive was scaled such that both experiments achieved similar Gurney velocity and strain rates (8600 s^{-1} in AM 316L vs. 9000 s^{-1} in wrought 304). The yield strength and tensile strength of wrought 304 stainless steel and AM 316L stainless steel are within 50-75 MPa of each other, and their failure strain ranges from 35-45% in both materials; see Table 1 for more details.

The fragment size distributions shown in Fig. 10 are similar, with mean fragment sizes of 7.38 ± 1.97 mm and 6.95 ± 2.47 mm for AM 316L and wrought 304, respectively. The fragment size distribution reported for this AM 316L should be considered an upper bound, based on the measurement method, which treats partially formed fragments as a single fragment and neglects crack spacing. The dynamic radiograph time of 60.12 µs allows fragments to fully separate and form free edges while reaching a near terminal velocity. At this time, there is minimal force driving further fragmentation; however, partial cracks may continue to propagate due to inertial loading. Another potential influence on the measurements is the limited spatial resolution of the dynamic radiograph (a point spread function of up to 500 µm was measured).

To understand the similarity in fragment size, despite the difference in shell manufacture methods, it is necessary to review the work of Mott [8], as refined by Grady [9]. Fracture nucleates at material defects—surface grooves in the AM 316L experiment—and release waves propagate away from these sites. The release waves prevent additional fractures from forming up to a critical distance, determined by the material density, applied strain rate, and fracture resistance. We conclude from the fragment size distribution in the AM 316L and wrought 304 shells that these properties are not significantly influenced by manufacturing methods.

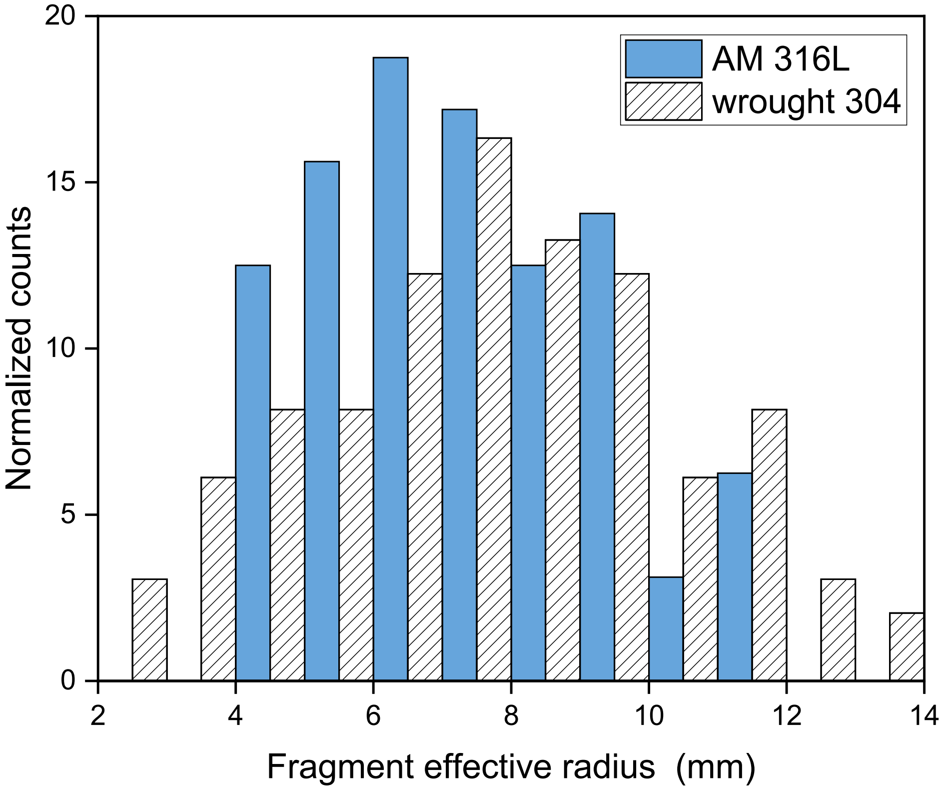

Fig. 10. Distributions of equivalent circular fragment radii of the AM 316L stainless steel spherical shell with surface defects and the wrought 304 stainless steel spherical shell from [32].

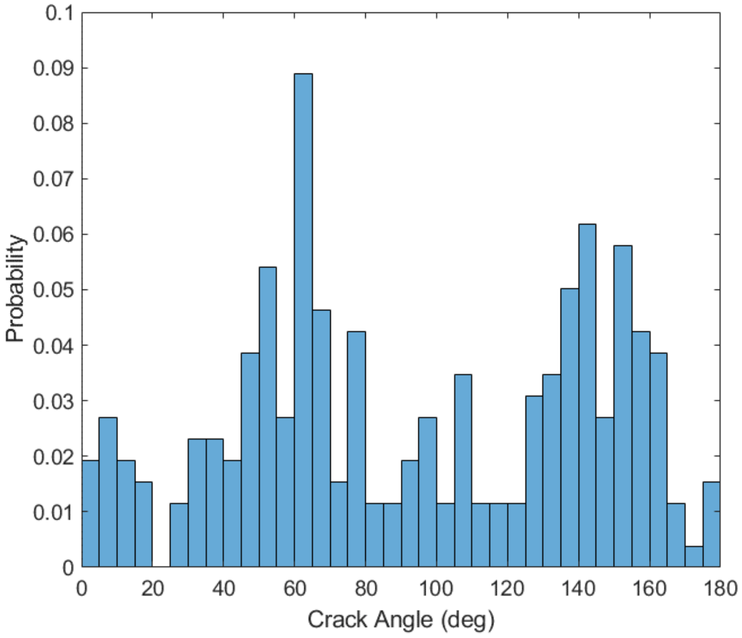

Fig 11. Probability distribution of crack orientation angle in the 2D radiograph plan. Crack angles range from 0 to 180 degrees, with 0 degrees corresponding to the 6 o'clock position in Fig. 6 and 7.

While less visually obvious in the radiograph compared to the optical images, it appears that there is preferential cracking along the perpendicular, cross-hatched surface grooves shown in Fig. 1. A probability distribution of crack orientation within the radiograph plane is shown in Fig 11. Crack angle probability is non-zero for nearly the full orientation range, indicating that crack angle was not solely directed by groove orientation. However, there are two peaks which appear to be separated by approximately 90 degrees, at 55 and 145 degrees, corresponding to the initial orthogonally oriented cracks observed at 36.6 μs in Fig. 7. There are also two smaller peaks at approximately 5 and 100 degrees suggesting a secondary set of orthogonal crack directions. While the surface groove patterns alone do not predict crack patterns and fragments shapes, the groove size and surface roughness measured clearly influences fragmentation behavior.

4.3 Fragmentation Analysis

Experimental results are analyzed to derive material properties of the AM 316L stainless steel and to facilitate comparison with dynamic experimental data from the literature.

4.3.1 Fragmentation Toughness

An analytical approach developed by Grady to assess fracture toughness is applied to the AM 316L stainless steel shell. This approach expands upon Mott's analysis of crack growth under dynamic conditions [8] by considering energy dissipated during the fracture process. Mott describes the fragmentation process in which the fracture minimum separation distance is dominated by the fracture release wave, the propagation of which is dependent on material properties. Grady relates this separation distance or fragment size to fragmentation toughness, K_f, noting that fragmentation toughness can be approximated by static fracture toughness in engineering alloys [9]. For a spherical shell loaded in biaxial tension, Grady derives the expression in Eq. 1 in which a_0 is the fragment area, $\dot{\varepsilon}$ is the applied biaxial tensile strain rate, referred to as stretching rate, and ρ and c are the material density and sound velocity.

$$a_0 = \left(\frac{\sqrt{12}K_f}{\rho c \bar{\dot{\varepsilon}}}\right)^{4/3} \qquad \text{Eq. 1}$$

Using the average fragment size from these calculations, along with other variables provided in Table 2, yields a fragmentation toughness of 174 MPa-m$^{1/2}$. Note that the stretching rate is estimated as V_r/R_0= 8600 s^{-1} using an average expansion velocity, V_r, of 1700 m/s and initial shell radius of R_0 = 198.05 mm, borrowing an expression from [78]. Assuming the same sound velocity and density for 304 stainless steel, the mean fragment area and stretching rate (9000 s^{-1}) yield a fragmentation toughness of 166 MPa-m$^{1/2}$ for the shell tested by Campbell *et al.* [32].

Table 2. Experimental and material parameters used to calculate fragmentation toughness.

fragment area, from experimental radiograph	a_0	14.8 mm^2
estimated stretching rate	$\dot{\varepsilon}$	8600 s^{-1}
density	ρ	8000 kg/m^3 [79]
longitudinal sound velocity	c	5750-5900 m/s [80]

Grady's approach was employed to compare fragmentation toughness values for different experiments performed at different strain rates. For 316L stainless steel, the fragment size is plotted as a function of stretching rate in Fig. 12. Here, a calculated fragment spacing, $x_0 = \sqrt{a_0}$, is used to facilitate comparisons with uniaxial dynamic experiments (i.e., ring and cylinder tests). Experimental results from dynamic cylinder expansion tests performed on AM and wrought 316L stainless steel are reported by Amott *et al*. [81] and included in Fig. 12. Similar failure strains achieved during gas gun loaded stainless steel cylinders and a discussion of failure along maximum shear planes can be found in the work of Rao et al. [82]. The AM 316L stainless steel has a similar fragmentation toughness to the wrought 304 shell and one of the AM 316L rings reported in [81]. The fragmentation toughness of the AM 316L shell is significantly lower than the wrought 316L rings and the other AM 316L ring and significantly higher than fragmentation toughness values of 80-100 MPa-m$^{1/2}$ reported by Grady and Kipp [12]. This may not be surprising given the experimental factors which can influence toughness at high strain rates, such as spall, surface finish, and microstructural defects.

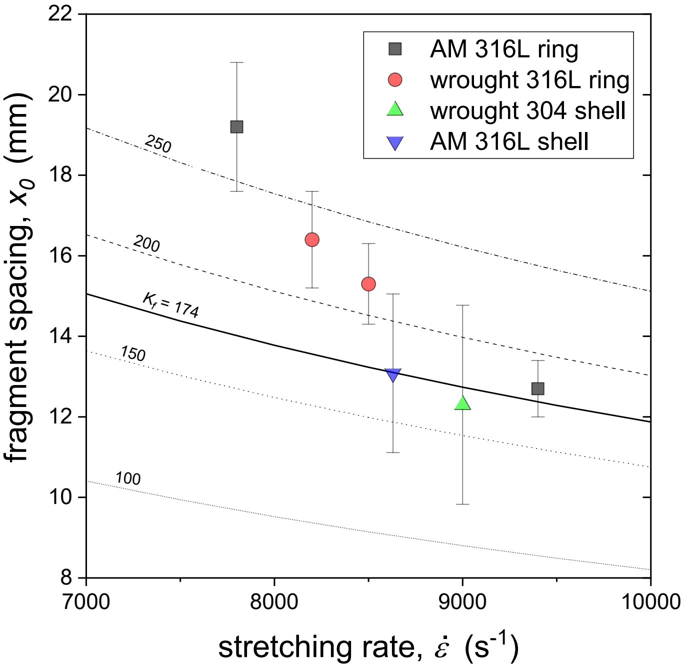

Fig. 12. Fragment size calculated based on Eq. 1, using parameters from Table 1, plotted vs. applied stretching rate.

4.3.2 Failure strain

In the previous section, the dominance of kinetic energy and fragment formation energy in determining fragment size were described. To extract more material-specific behavior, an analysis of failure strain is performed using a geometric argument.

Recall the initial outer radius of curvature, R_0 = 201 mm. Integrating the velocity at Probe 1 and Probe 4 yields a theoretical radius (Fig. 13). The time of fracture was estimated based on visual indication of cracks at the shell surface (28.6-32.6 µs per Fig. 8) and the shell radius at time of failure is $R_f \sim$ 230 mm (Fig. 13). The average true tensile strain at failure can be calculated based on spherical expansion by $\varepsilon_t = -2ln(R_0/R_f)$, see [78, 83] for further analysis, or direct measurement of fragment thinning, $\varepsilon_t = \frac{1}{2}ln(t_0/t_f)$, as applied in [32]. A tensile failure strain of

27% was calculated using the first method and, conserving mass, the latter method yields an average fragment thickness of 1.7 mm.

For 304 stainless steel, an average fragment thickness of 1.4 mm yielded a true tensile failure strain of 38% [32]. It is reasonable to conclude that shell fragmentation initiated at surface groove stress concentrations, from the crack pattern orientation observed in Fig. 7 and 11. Hence, an earlier failure time translates to a lower strain at failure.

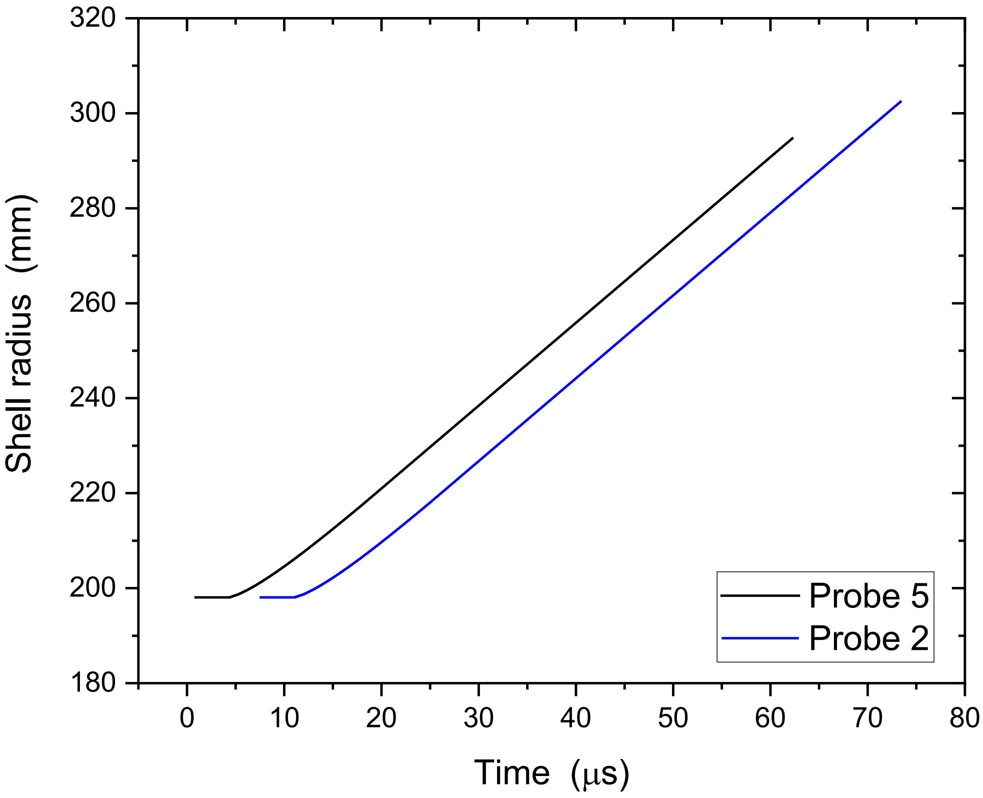

Fig. 13. Integrated velocity measured via PDV probes near the center and edge of the spherical shell during expansion.

4.4 Comparison of AM to Wrought Stainless Steel

A comparison of fragmentation toughness and failure strain compared with other reported values in the literature is provided in Table 3. The measured spall strength for AM 316L stainless steel ($\sigma_{spall} = 3.4$ GPa, [58]) is in good agreement with the current experiment, in which $\sigma_{spall} = 3.2$ GPa was calculated using the measured pullback velocity ($\Delta u_{pb} = 139$ m/s, Fig. 8) and Eq. 2 from [84].

$$\sigma_{spall} = \frac{1}{2}\rho c \Delta u_{pb} \qquad \text{Eq. 2}$$

Table 3. Comparison of fragmentation toughness and failure strain measurements reported in literature.

Material	Experimental configuration	Stretching rate (s^{-1})	Fragmentation toughness (fracture toughness denoted by K_{IC}) in MPa-m$^{1/2}$	Tensile failure strain	Reference
AM 316L	ASTM E8/E8M-11, ASTM-647-15 and ASTM-399-12	10^{-3}	112–278	0.40-0.45	[85-87]
Wrought 304	Ball on plate impact	~10^{3}	80-100	0.38	[12]
Wrought 304	Spherical shell	9000	166	0.38	[32]
AM 316L	Spherical shell	8630	174	0.27	Current experiment
AM 316L	Cylinder	7800, 9400	230	0.35, 0.20	[81]
Wrought 316L	Cylinder	8200, 8500	219	0.19, 0.23	[81]

Despite the surface grooves, the additively manufactured 316L stainless steel performs within the expected performance envelope (i.e., tensile failure strain and fragmentation toughness) of wrought 316L and 304 stainless steels under hydrodynamic loading. It is reasonable that the surface grooves do not dominate fragmentation behavior given the high strain-hardening and strain-to-failure typical of AM 316L stainless steel [88, 89]. In a fatigue loading scenario, the critical flaw size of AM 316L stainless steel can be approximated as 7 mm, based on $a_c = \frac{1}{\pi}\left(\frac{K_f}{\sigma_y}\right)^2$ per [90], where the yield stress, σ_y~600 MPa [89] .

5. Conclusions

A 316L stainless steel spherical shell was produced by laser powder bed additive manufacturing and partial machining, leaving support structure grooves at the convex outer surface. The shell was tested under explosively driven biaxial tension to observe the behavior of AM 316L stainless steel and to assess the effect of AM surface grooves on fragmentation behavior. Analytical calculations based on an energy balance approach yield an average fragmentation toughness value of 174 MPa-m$^{1/2}$. Based on the fragment spacing, as measured by a single radiograph acquired 60.12 µs after detonation trigger and visual indication of crack nucleation time of 28.6-32.6 µs acquired by high-speed imaging, an average tensile failure strain of 0.27 was determined. While the fragmentation toughness and fragment size are comparable to those calculated and measured for wrought 304 tested under similar conditions, the failure strain is significantly lower than 0.38 reported for wrought 304. The decrement in failure strain is attributed to early failure at the surface groove stress concentrations, as supported by visual indication from high-speed photography and fragment directionality from radiographic analysis.

Considering the similarity in fragment size/fragmentation toughness coupled with the relative ease of manufacturability offered by the laser powder bed AM process with minimal finish machining—surface grinding as opposed to lathe turning—AM appears to be a reasonable manufacturing approach for high-strain rate applications.

Acknowledgments

We gratefully acknowledge Phillip Miller, Christopher Tomkins, Isaac Martinez, Kevin Wabick, Garret Tousley, Brian Esquibel, John Wilson, Timothy Byers, Andrew McNutt, Evan Anderson, and Wendy McNeil, from M-3 Focused Experiments group at the Los Alamos National Laboratory for the support and fielding of this hydrodynamic test. This research has benefitted from technical discussions and guidance provided by Kenneth Eckelmeyer and Gail Glendinning.

This work was performed under the auspices of the U.S. Department of Energy by Lawrence Livermore National Laboratory under contract DE-AC52-07NA27344. This article has been assigned the release ID #LLNL-JRNL-841186.

References

1. Griffith, A.A., *The phenomena of rupture and flow in solids.* Philosophical Transactions of the Royal Society of London, 1921. **Series A, Containing Papers of a Mathematical or Physical Character**(221): p. 163-198.
2. Lawn, B., *Fracture of brittle solids*. 2nd ed, ed. E.A. Davis and I.M. Ward. 1998, United Kingdom: University Press, Cambridge.
3. Brocks, W., A. Cornec, and I. Scheider, *Computational aspects of nonlinear fracture mechanics*. 2003, Pergamon: Boston.
4. Ritchie, R.O., J.F. Knott, and J.R. Rice, *Relationship between critical tensile stress and fracture toughness in mild-steel.* Journal of the Mechanics and Physics of Solids, 1973. **21**(6): p. 395-410.
5. Needleman, A., *A continuum model for void nucleation by inclusion debonding.* Journal of Applied Mechanics-Transactions of the Asme, 1987. **54**(3): p. 525-531.
6. Tvergaard, V. and A. Needleman, *Analysis of the cup-cone fracture in a round tensile bar.* Acta Metallurgica, 1984. **32**(1): p. 157-169.
7. Gurson, A.L., *Continuum theory of ductile rupture by void nucleation and growth. 1. Yield criteria and flow rules for porous ductile media.* Journal of Engineering Materials and Technology-Transactions of the Asme, 1977. **99**(1): p. 2-15.
8. Mott, N.F., *Fragmentation of shell cases.* Proceedings of the Royal Society of London Series a-Mathematical and Physical Sciences, 1947. **189**(1018): p. 300-308.
9. Grady, D., *Fragmentation of rings and shells: The legacy of N. F. Mott*. 1 ed. Shock wave and high pressure phenomena, ed. L. Davidson, Y. Horie, and R.A. Graham. 2006: Springer-Verlag, Berlin.
10. Grady, D.E., M.E. Kipp, and D. Benson, *Energy and statistical effects in the dynamic fragmentation of metal rings*, in *Mechanical Properties at High Rates of Strain*, J. Harding, Editor. 1984, Institute of Physics: Bristol.
11. Kipp, M.E. and D.E. Grady, *Dynamic fracture growth and interaction in one dimension.* Journal of the Mechanics and Physics of Solids, 1985(33): p. 399-415.
12. Grady, D.E. and M.E. Kipp, *Impact failure and fragmentation properties of metals*. 1998, Sandia National Laboratories.

13. Grady, D.E. and M.E. Kipp, *Fragmentation properties of metals.* International Journal of Impact Engineering, 1997. **20**: p. 293-308.
14. Grady, D.E. and M.E. Kipp, *Dynamic Fracture and Fragmentation*, in *High-Pressure Shock Compression of Condensed Matter*, J.R. Asay and M. Shahinpoor, Editors. 1993, Springer: New York, NY.
15. Botvina, L.R. and A.V. Larionova, *Dynamic fragmentation in steel cylindrical shells.* Engineering Fracture Mechanics, 2022. **269**: p. 16.
16. Goto, D.M., et al., *Investigation of the fracture and fragmentation of explosively driven rings and cylinders.* International Journal of Impact Engineering, 2008. **35**(12): p. 1547-1556.
17. Zhu, J.J., et al., *Axial distribution of fragments from the dynamic explosion fragmentation of metal shells.* International Journal of Impact Engineering, 2019. **123**: p. 140-146.
18. Stronge, W.J., X.Q. Ma, and L.T. Zhao, *Fragmentation of explosively expanded steel cylinders.* International Journal of Mechanical Sciences, 1989. **31**(11-12): p. 811-&.
19. Hoggatt, C.R. and R.F. Recht, *Fracture Behavior of Tubular Bombs.* Journal of Applied Physics, 1968. **39**(3): p. 1856-1862.
20. Al-Hassani, S.T.S., H.G. Hopkins, and W. Johnson, *A note on the fragmentation of tubular bombs.* International Journal of Mechanical Sciences, 1969. **11**(6): p. 545-549.
21. Gurney, R.W., *The initial velocities of fragments from bombs, shell, and grenades*. 1943, Ballistic Research Laboratories: Aberdeen Proving Ground, MD.
22. Jones, G.E., J.E. Kennedy, and L.D. Bertholf, *Ballistics calculations of R. W. Gurney.* American Journal of Physics, 1980. **48**(4): p. 264-269.
23. Batchelor, G.K. and R.E. Street, *The Scientific Papers of Sir Geoffrey Ingram Taylor.* Physics Today, 1961. **14**(1): p. 60-62.
24. Neel, C., et al., *Conical impact fragmentation test (CIFT).* International Journal of Impact Engineering, 2020. **140**: p. 6.
25. Grady, D., *Investigation of Explosively Driven Fragmentation of Metals-Two-Dimensional Fracture and Fragmentation of Metal Shells: Progress Report II*. 2003: Lawrence Livermore National Laboratory.
26. McGlaun, J.M., S.L. Thompson, and M.G. Elrick, *CTH - A 3-Dimensional shock-wave physics code.* International Journal of Impact Engineering, 1990. **10**(1-4): p. 351-360.
27. Trucano, T.G., D.E. Grady, and J.M. McGlaun, *Fragmentation statistics from Eulerian hydrocode calculations.* International Journal of Impact Engineering, 1990. **10**(1-4): p. 587-600.
28. Lippard, H.E., et al., *Microsegregation behavior during solidification and homogenization of AerMet100 steel.* Metallurgical and Materials Transactions B-Process Metallurgy and Materials Processing Science, 1998. **29**(1): p. 205-210.
29. Wilson, L.T., et al. *Comparison of calculated and experimental results of fragmenting cylinder experiments*. in *International Conference on Fundamental Issues and Applications of Shock-Wave and High-Strain-Rate Phenomena (EXPLOMET 2000)*. 2000. Los Almos Natl Lab, Albuquerque, Nm: Elsevier Science Bv.
30. Syn, C.K., et al., *Plastic deformation and fracture of steels under dynamic biaxial loading*. 2004: Lawrence Livermore National Laboratory.
31. Tsuji, P., et al., *Embedded smoothed particle hydrodynamics.* Computer Methods in Applied Mechanics and Engineering, 2020. **366**: p. 16.
32. Campbell, G.H., et al., *Fragmentation in biaxial tension.* Journal of Applied Physics, 2007. **101**(3): p. 10.
33. Hopson, M.V., C.M. Scott, and R. Patel, *Computational comparisons of homogeneous and statistical descriptions of AerMet100 steel subjected to high strain rate loading.* International Journal of Impact Engineering, 2011. **38**(6): p. 451-455.

34. Lambert, D.E., et al., *Explosively Driven Fragmentation Experiments for Continuum Damage Modeling.* Journal of Pressure Vessel Technology-Transactions of the ASME, 2012. **134**(3): p. 7.
35. Kong, X.S., et al., *A numerical investigation on explosive fragmentation of metal casing using Smoothed Particle Hydrodynamic method.* Materials & Design, 2013. **51**: p. 729-741.
36. Dong, X.L., et al. *Adiabatic shearing failure of explosively driven metallic cylinder shell, from experiments to simulation*. in *11th International Conference on the Mechanical and Physical Behaviour of Materials under Dynamic Loading (DYMAT)*. 2015. Lugano, SWITZERLAND: E D P Sciences.
37. Vafadar, A., et al., *Advances in Metal Additive Manufacturing: A Review of Common Processes, Industrial Applications, and Current Challenges.* Applied Sciences-Basel, 2021. **11**(3): p. 31.
38. Gisario, A., et al., *Metal additive manufacturing in the commercial aviation industry: A review.* Journal of Manufacturing Systems, 2019. **53**: p. 124-149.
39. Gardner, L., *Metal additive manufacturing in structural engineering-review, advances, opportunities and outlook.* Structures, 2023. **47**: p. 2178-2193.
40. Chowdhury, S., et al., *Laser powder bed fusion: a state-of-the-art review of the technology, materials, properties & defects, and numerical modelling.* Journal of Materials Research and Technology-Jmr&T, 2022. **20**: p. 2109-2172.
41. Narasimharaju, S.R., et al., *A comprehensive review on laser powder bed fusion of steels: Processing, microstructure, defects and control methods, mechanical properties, current challenges and future trends.* Journal of Manufacturing Processes, 2022. **75**: p. 375-414.
42. Yusuf, S.M., S. Cutler, and N. Gao, *Review: The Impact of Metal Additive Manufacturing on the Aerospace Industry.* Metals, 2019. **9**(12): p. 35.
43. Allison, F.E. and J.T. Schriempf, *Explosively Loaded Metallic Cylinders. II.* Journal of Applied Physics, 2004. **31**(5): p. 846-851.
44. Allison, F.E. and R.W. Watson, *Explosively Loaded Metallic Cylinders. I.* Journal of Applied Physics, 2004. **31**(5): p. 842-845.
45. Johnson, G.R. and W.H. Cook, *Fracture characteristics of 3 metals subjected to various strains, strain rates, temperatures and pressures.* Engineering Fracture Mechanics, 1985. **21**(1): p. 31-48.
46. Li, C.Y., et al., *Phase field fracture in elasto-plastic solids: Incorporating phenomenological failure criteria for ductile materials.* Computer Methods in Applied Mechanics and Engineering, 2022. **391**: p. 29.
47. Nagesh, C. and N.K. Gupta, *Large deformations and failure of clamped circular steel plates under uniform impulsive loads using various phenomenological damage models.* International Journal of Impact Engineering, 2022. **166**: p. 104255.
48. Nahrmann, M. and A. Matzenmiller, *Modelling of nonlocal damage and failure in ductile steel sheets under multiaxial loading.* International Journal of Solids and Structures, 2021. **232**: p. 14.
49. Bonneric, M., C. Brugger, and N. Saintier, *Investigation of the sensitivity of the fatigue resistance to defect position in aluminium alloys obtained by Selective laser melting using artificial defects.* International Journal of Fatigue, 2020. **134**: p. 11.
50. Weck, A., et al., *Visualization by X-ray tomography of void growth and coalescence leading to fracture in model materials.* Acta Materialia, 2008. **56**(12): p. 2919-2928.
51. Cai, W., et al., *Microstructure evolution and fracture behaviour of TWIP steel under dynamic loading.* Materials Science and Engineering a-Structural Materials Properties Microstructure and Processing, 2022. **851**: p. 11.
52. Gilman, J.J., *Propagation of cleave cracks in crystals.* Journal of Applied Physics, 1956. **27**(11): p. 1262-1269.
53. Freund, L.B. and J.W. Hutchinson, *High strain-rate crack-growth in rate-dependent plastic solids.* Journal of the Mechanics and Physics of Solids, 1985. **33**(2): p. 169-191.

54. Remington, B.A., et al., *Rayleigh-Taylor instabilities in high-energy density settings on the National Ignition Facility.* Proceedings of the National Academy of Sciences of the United States of America, 2019. **116**(37): p. 18233-18238.
55. Liang, M.Z., X.Y. Li, and F.Y. Lu, *Effects of U-notches on the dynamic fracture and fragmentation Of explosively driven cylinders.* Theoretical and Applied Fracture Mechanics, 2015. **77**: p. 50-58.
56. Wood, P., et al., *High strain rate effect on tensile ductility and fracture of AM fabricated Inconel 718 with voided microstructures.* Materials & Design, 2021. **208**: p. 18.
57. Fick, J.P.M., K.T. Ramesh, and P.K. Swaminathan, *Modeling of ductile fragmentation that includes void interactions.* Journal of the Mechanics and Physics of Solids, 2015. **85**: p. 54-73.
58. Koube, K.D., et al., *An assessment of spall failure modes in laser powder bed fusion fabricated stainless steel 316L with low-volume intentional porosity.* Journal of Applied Physics, 2023. **133**: p. 185903.
59. Koube, K.D., et al., *Spall damage mechanisms in laser powder bed fabricated stainless steel 316L.* Materials Science and Engineering a-Structural Materials Properties Microstructure and Processing, 2022. **851**: p. 12.
60. Lamb, K., et al., *Anisotropic spall failure of additively manufactured 316L stainless steel.* Additive Manufacturing, 2023. **66**: p. 13.
61. Buchar, J., S. Role, and J. Hrebicek, *Strain rate dependence of the spall strength of steels.* Journal De Physique Iv, 1997. **7**(C3): p. 951-956.
62. Mills, W.J., *Fracture toughness of type 304 and 316 stainless steels and their welds.* International Materials Reviews, 1997. **42**(2): p. 45-82.
63. Garlea, E., et al., *Variation of elastic mechanical properties with texture, porosity, and defect characteristics in laser powder bed fusion 316L stainless steel.* Materials Science and Engineering a-Structural Materials Properties Microstructure and Processing, 2019. **763**: p. 15.
64. Davies, C.M., et al. *Fracture toughness behavior of 316L stainless steel samples manufactured through selective laser melting*. in *ASME Pressure Vessels and Piping Conference (PVP 2018)*. 2018. Prague, CZECH REPUBLIC.
65. Wang, X.L., et al., *Crystallographic orientation dependence of Charpy impact behaviours in stainless steel 316L fabricated by laser powder bed fusion.* Additive Manufacturing, 2021. **46**.
66. de Sonis, E., et al., *Microstructure-Toughness relationships in 316L stainless steel produced by laser powder bed fusion.* Materials Science and Engineering a-Structural Materials Properties Microstructure and Processing, 2023. **877**.
67. Riemer, A., et al., *On the fatigue crack growth behavior in 316L stainless steel manufactured by selective laser melting.* Engineering Fracture Mechanics, 2014. **120**: p. 15-25.
68. Carlton, H.D., et al., *Damage evolution and failure mechanisms in additively manufactured stainless steel.* Materials Science and Engineering a-Structural Materials Properties Microstructure and Processing, 2016. **651**: p. 406-414.
69. Lavery, N.P., et al., *Effects of hot isostatic pressing on the elastic modulus and tensile properties of 316L parts made by powder bed laser fusion.* Materials Science and Engineering a-Structural Materials Properties Microstructure and Processing, 2017. **693**: p. 186-213.
70. Li, W.P., et al., *Plastically heterogeneity-driven fracture in additive manufactured steels.* Engineering Fracture Mechanics, 2023. **283**: p. 17.
71. Chao, Q., et al., *The effect of post-processing heat treatment on the microstructure, residual stress and mechanical properties of selective laser melted 316L stainless steel.* Materials Science and Engineering a-Structural Materials Properties Microstructure and Processing, 2021. **821**.
72. Li, Z., et al., *Tensile properties, strain rate sensitivity, and activation volume of additively manufactured 316L stainless steels.* International Journal of Plasticity, 2019. **120**: p. 395-410.

73. Smith, W.L., et al., *Residual stress analysis of in situ surface layer heating effects on laser powder bed fusion of 316L stainless steel.* Additive Manufacturing, 2021. **47**: p. 12.
74. DePiero, S.C. and D.M. Hoffman, *Formulation and characterization of LX-17-2 from new FK 800 binder and WA, ATK, and BAE TATBs*. 2009: Lawrence Livermore National Laboratory.
75. Colville, J.C., *LX-17 and LX-10 Test Data*. 1992, Pantex Plant.
76. Legland, D., I. Arganda-Carreras, and P. Andrey, *MorphoLibJ: integrated library and plugins for mathematical morphology with ImageJ.* Bioinformatics, 2016. **32**(22): p. 3532-3534.
77. Schindelin, J., et al., *Fiji: an open-source platform for biological-image analysis.* Nature Methods, 2012. **9**(7): p. 676-682.
78. Huang, Z.W. and X.L. Yu, *Numerical Simulation Study of Expanding Fracture of 45 Steel Cylindrical Shell under Different Detonation Pressure.* Materials, 2022. **15**(11): p. 16.
79. *Metals Handbook Tenth Edition*, in *Specialty Steels and Heat-Resistant Alloys*. 1990, ASM International. p. 871.
80. Kim, C., et al., *Ultrasonic nondestructive evaluation of laser powder bed fusion 316L stainless steel.* Additive Manufacturing, 2021. **38**: p. 12.
81. Amott, R., et al. *The Fracture and Fragmentation Behaviour of Additively Manufactured Stainless Steel 316L*. in *19th Biennial American-Physical-Society (APS) Conference on Shock Compression of Condensed Matter (SCCM)*. 2015. Tampa, FL: Amer Inst Physics.
82. Rao, P., et al., *Fragmentation studies by non-explosive cylinder expansion technique.* International Journal of Impact Engineering, 2020. **146**: p. 10.
83. Anderson, C.E., W.W. Predebon, and R.R. Karpp, *Computational modeling of explosive-filled cylinders.* International Journal of Engineering Science, 1985. **23**(12): p. 1317-1330.
84. Luo, S.N., et al., *Laser-induced shock waves in condensed matter: Some techniques and applications.* High Pressure Research, 2004. **24**(4): p. 409-422.
85. Tolosa, I., et al., *Study of mechanical properties of AISI 316 stainless steel processed by "selective laser melting", following different manufacturing strategies.* International Journal of Advanced Manufacturing Technology, 2010. **51**(5-8): p. 639-647.
86. Boyer, H., *Atlas of fatigue curves, ASM International, 1986.* 7 Bibliography 7 Bibliography, 2015.
87. Suryawanshi, J., K.G. Prashanth, and U. Ramamurty, *Mechanical behavior of selective laser melted 316L stainless steel.* Materials Science and Engineering a-Structural Materials Properties Microstructure and Processing, 2017. **696**: p. 113-121.
88. Torabi, A.R., et al., *Mixed mode I-III fracture resistance of stainless steel 316L weakened by V-notches with end holes.* Theoretical and Applied Fracture Mechanics, 2022. **122**: p. 20.
89. Yang, Y.Y., et al., *Densification, surface morphology, microstructure and mechanical properties of 316L fabricated by hybrid manufacturing.* International Journal of Advanced Manufacturing Technology, 2018. **97**(5-8): p. 2687-2696.
90. Crawford, R.J., *Chapter 2 - Mechanical Behaviour of Plastics*, in *Plastics Engineering*. 1998. p. 41-167.